We are IntechOpen, the world's leading publisher of Open Access books
Built by scientists, for scientists

6,900
Open access books available

185,000
International authors and editors

200M
Downloads

Our authors are among the

154
Countries delivered to

TOP 1%
most cited scientists

12.2%
Contributors from top 500 universities

WEB OF SCIENCE™

Selection of our books indexed in the Book Citation Index in Web of Science™ Core Collection (BKCI)

Interested in publishing with us?
Contact book.department@intechopen.com

Numbers displayed above are based on latest data collected.
For more information visit www.intechopen.com

Chapter 4

Shape Optimization of Busemann-Type Biplane Airfoil for Drag Reduction Under Non-Lifting and Lifting Conditions Using Genetic Algorithms

Yi Tian and Ramesh K. Agarwal

Additional information is available at the end of the chapter

http://dx.doi.org/10.5772/62811

Abstract

The focus of this chapter is on the shape optimization of the Busemann-type biplane airfoil for drag reduction under both non-lifting and lifting conditions using genetic algorithms. The concept of biplane airfoil was first introduced by Adolf Busemann in 1935. Under design conditions at a specific supersonic flow speed, the Busemann biplane airfoil eliminates all wave drag due to its symmetrical biplane configuration; however, it produces zero lift. Previous research has shown that the original Busemann biplane airfoil shows a poor performance under off-design conditions. In order to address this problem of zero lift and to improve the off-design-condition performance, shape optimization of an asymmetric biplane airfoil is performed. The commercially available computational fluid dynamics (CFD) solver ANSYS FLUENT is employed for computing the inviscid supersonic flow past the biplane airfoil. A single-objective genetic algorithm (SOGA) is employed for shape optimization under the non-lifting condition to minimize the drag, and a multi-objective genetic algorithm (MOGA) is used for shape optimization under the lifting condition to maximize both the lift and the lift-to-drag ratio. The results obtained from both SOGA and MOGA show a significant improvement in the design and off-design-condition performance of the optimized Busemann biplane airfoil compared to the original airfoil.

Keywords: genetic algorithm, shape optimization, biplane airfoil, computational fluid dynamics, supersonic flow

INTECH
open science | open minds

© 2016 The Author(s). Licensee InTech. This chapter is distributed under the terms of the Creative Commons Attribution License (http://creativecommons.org/licenses/by/3.0), which permits unrestricted use, distribution, and reproduction in any medium, provided the original work is properly cited. CC BY

1. Introduction

For decades, the speed of commercial aircrafts has been bounded by the sound barrier. Even the most successful supersonic transport (SST) plane, the Concorde, could only be deployed in very few routes due to government regulation, low efficiency, and excessive noise generation. Since the retirement of Concorde in 2003, the desire for developing a replacement for Concorde space still remains. In order to accomplish that, one of the biggest design challenges is to eliminate, or at least greatly reduce, the strong bow shock wave generated during supersonic flight, which can cause high wave drag and substantial noise. At supersonic speed, a bow shock is generated ahead of the airplane. This shock wave generates a substantially high wave drag which needs to be overcome by the engine by providing a much higher thrust compared to that for a conventional subsonic/transonic airplane, which results in higher fuel consumption and low propulsive efficiency. In order to address the high-wave-drag problem at supersonic speed, a biplane concept was proposed by Adolf Busemann in 1935 [1] which can potentially avoid the formation of bow shock and thus does not create sonic boom.

During the period from 1935 to 1960, substantial research was conducted on the Busemann biplane concept. Moeckel [2] and Licher [3] performed the theoretical analysis of the optimized lifting supersonic biplanes. Tan [4] took a further step and derived analytical expressions for the drag and lift of a three-dimensional supersonic biplane with a finite span of rectangular plan form. Some experimental results were obtained by Ferri [5] using a wind tunnel, and comparisons were made between the experimental and analytical results. During the past 10 years, considerable interest has been shown in supersonic biplane airfoils. Igra and Arad [6] tested and analyzed the effects of different parameters on the drag coefficient of the Busemann airfoil under various flow conditions. Kusunose et al. [7] proposed a concept for the next-generation supersonic transport using the Busemann biplane design. A series of studies using both computational fluid dynamics (CFD) and wind-tunnel experimental methods have been completed by Kusunose's research group [7–16].

Recently, Hu et al. [17] employed a multi-point adjoint-based aerodynamic design and optimization method to improve the baseline Busemann biplane airfoil's off-design performance and alleviate the flow-hysteresis problem. They also addressed the problem of minimizing its drag by shape optimization. This chapter addresses the aerodynamic shape optimization of two-dimensional symmetric Busemann biplane airfoil under both design and off-design conditions for reducing its wave drag, and the alleviation of the flow-hysteresis and choked-flow effects using a single-objective genetic algorithm. The symmetric Busemann biplane airfoil generates zero lift; this problem is addressed by introducing asymmetry in the shape of two profiles of the biplane. The asymmetric configuration is shape optimized for maximum lift and minimum drag by employing a multi-objective genetic algorithm. The flow field is computed using the commercial CFD software ANSYS FLUENT. Body-fitted H-grids around the airfoils are generated using the ICEM software. Random airfoil shapes with constraints in a given generation of the genetic algorithm are obtained using the Bezier curves (third-order polynomials).

http://dx.doi.org/10.5772/62811

2. Flow field simulation of the standard diamond-shaped airfoil and the baseline Busemann biplane airfoil under design and off-design conditions

The flow fields of both the standard diamond-shaped airfoil and the Busemann biplane airfoil are computed at zero angle of attack (the zero-lift condition). For meaningful comparison, the total thickness of the two airfoils is set to be equal. For this specific case under consideration, the thickness-to-chord ratio of the diamond-shaped airfoil is $t/c = 0.1$, while the thickness-to-cho rd ratio of the Busemann airfoil is $t/c = 0.05$ for both its upper and lower components. The distance between the upper and lower components of the Busemann airfoil is set to be one half of the chord length to obtain the theoretical minimum drag under the design condition at Mach number $M = 1.7$. The angle of attack is set to be 0 as we first consider the non-lifting design and off-design conditions by varying the Mach number below 1.7 and greater than 1.7.

2.1. Mesh generation

The commercial meshing software ANSYS ICEM CFD is used to generate the mesh for computing the flow field. The far-field boundary is set at 21 chord length by a 20.5-chord-length rectangle from the center of the airfoil. **Figure 1** shows the H-mesh configuration generated for the simulations. There are 64 nodes around the two components both horizontally and vertically. In between the two components, the grid has a dimension of 32 nodes (vertically) × 64 nodes (horizontally). An ICEM replay script file is created to automatically generate the mesh for the flow past different airfoil shapes once it is called.

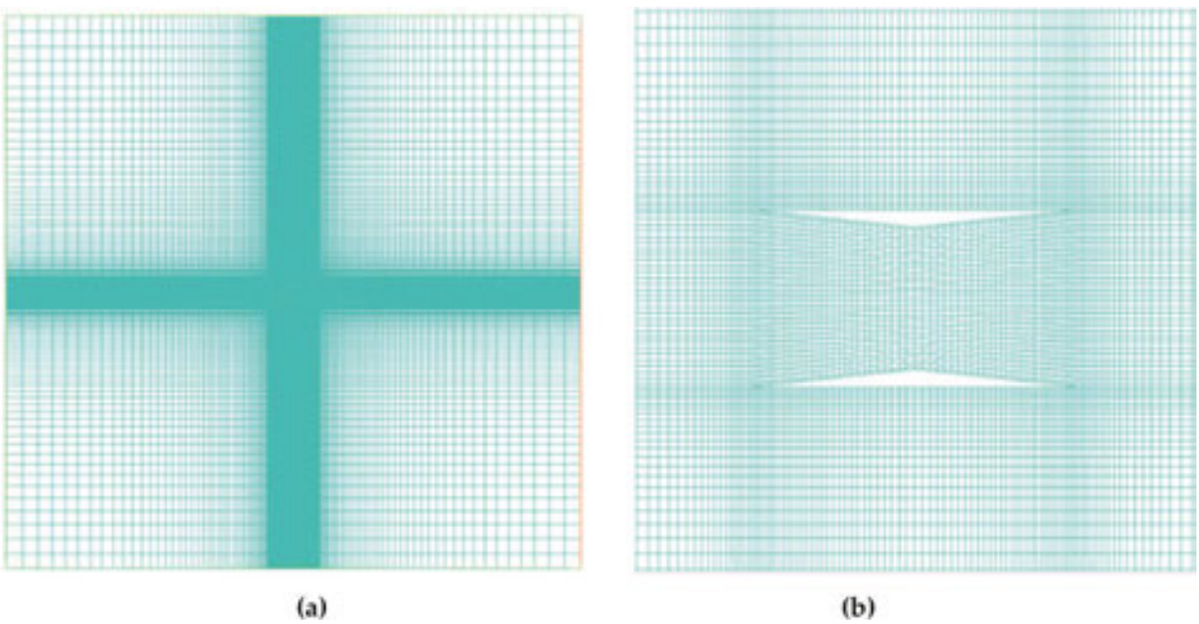

Figure 1. (a) H-mesh generated in the computational domain and (b) zoomed-in view of the mesh near the biplane airfoil.

2.2. Steady-state flow field simulation at $M < 1.7$

As has been mentioned above, the baseline Busemann biplane airfoil has a much lower drag under its design condition at Mach number $M = 1.7$. However, it shows a poor aerodynamic performance under off-design conditions, which may cause much higher drag compared to the standard diamond-shaped airfoil. The configurations of both the standard diamond-shaped airfoil and the baseline Busemann biplane airfoil are shown in **Figure 2**.

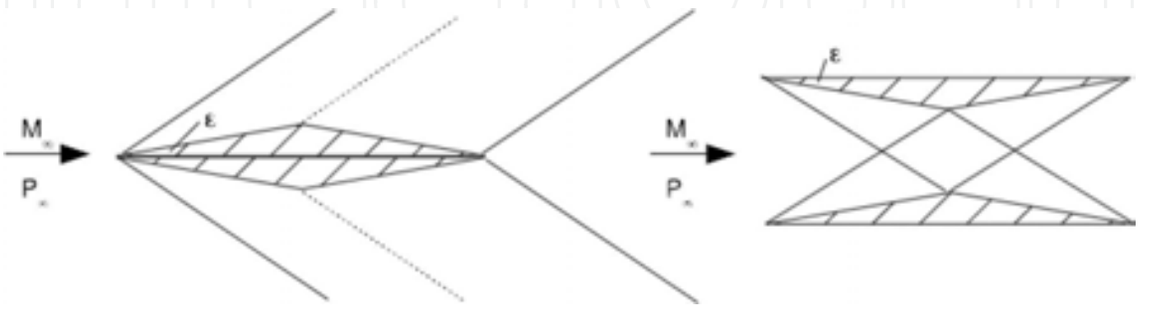

Figure 2. Configurations of standard diamond-shaped airfoil (left) and baseline Busemann biplane airfoil (right).

Figure 3 shows the drag coefficient c_d of both the standard diamond-shaped airfoil and the baseline Busemann biplane airfoil under the zero-lift condition over a range of Mach numbers ($0.3 \leq M \leq 3.3$). The simulations are performed using ANSYS FLUENT; the flow field is initialized with an impulsive uniform flow.

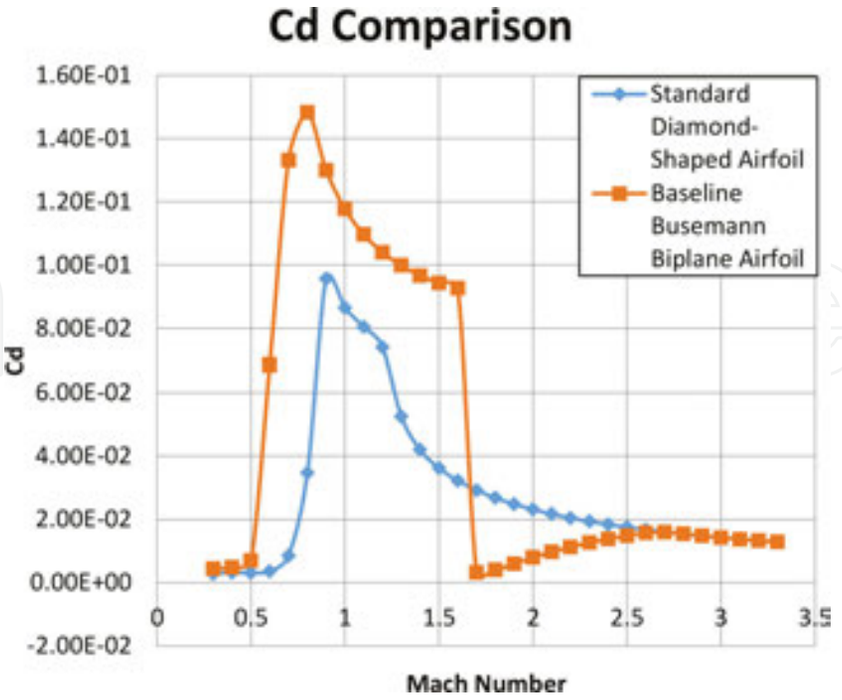

Figure 3. Comparison of C_d for two different airfoils under non-lifting condition.

http://dx.doi.org/10.5772/62811

As shown in **Figure 3**, the baseline Busemann biplane airfoil has a higher drag compared to the standard diamond-shaped airfoil when the Mach number is low ($0.3 \leq M \leq 1.6$). In the range of $1.7 \leq M \leq 2.7$, however, the drag generated by the baseline Busemann biplane airfoil is smaller than that generated by the standard diamond-shaped airfoil, especially at $M = 1.7$ which is the design condition for the Busemann airfoil. **Figure 3** demonstrates the advantage of the Busemann biplane airfoil as it produces much lower drag near its design condition ($M = 1.7$) due to the wave-reduction and wave-cancellation effects. The simulations shown above demonstrate that the baseline Busemann biplane airfoil shows a very good performance under its design conditions ($M = 1.7$), while it has a much higher drag under off-design conditions due to the choked-flow phenomenon at lower Mach numbers ($M < 1.7$). **Figure 4(a)** through **4(d)** shows the flow field around the baseline Busemann biplane airfoil under two different off-design conditions, both of which result in high drag but due to different reasons. At $M = 0.8$, as shown in **Figure 4(a)**, the flow between the two airfoil components reaches Mach 1 at the mid-chord of the airfoil, and then increases further downstream to supersonic flow. After reaching the trailing edge of the airfoil, however, the flow speed drops to subsonic and hence forms a vertical shock wave. The supersonic flow in the rear part of the airfoil (after the mid-point) creates a low-pressure region, as shown in **Figure 4(b)**, which leads to a higher wave drag ($c_d = 0.148$) at this off-design condition of $M = 0.8$. At $M = 1.6$, however, as shown in **Figure 4(c)**, the flow field is very different from that at $M = 0.8$ under subsonic conditions. A bow shock is formed in front of the leading edge of the airfoil. The flow speed drops to subsonic and a high-pressure region, as shown in **Figure 4(d)**, is created which again generates a high drag ($c_d = 0.0926$).

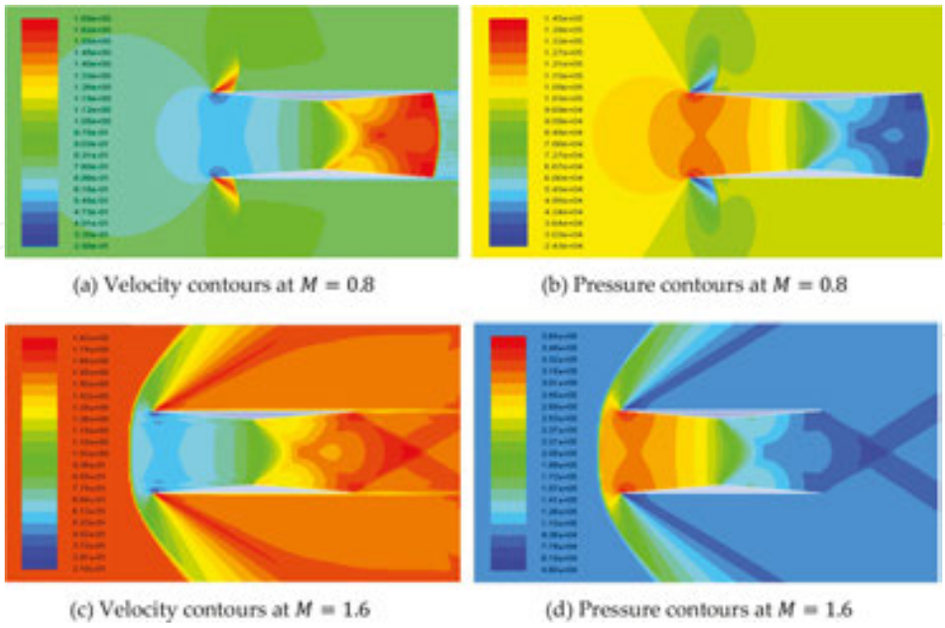

Figure 4. Velocity and pressure contours around the baseline Busemann airfoil: (a) velocity contours at $M = 0.8$, (b) pressure contours at $M = 0.8$, (c) velocity contours at $M = 1.6$, (d) pressure contours at $M = 1.6$.

2.3. Flow field simulation during acceleration and deceleration

Despite the high drag being generated under off-design conditions, there is an even worse problem caused by the flow-hysteresis phenomenon during acceleration and choked-flow phenomenon during deceleration that need to be addressed under off-design conditions. To demonstrate these phenomena, flow field simulations are conducted under both acceleration and deceleration using the previous simulation results shown in **Figure 4** as the initial condition. **Figure 5** shows two separated c_d curves during acceleration and deceleration of the biplane airfoil. As shown in **Figure 5**, the change in acceleration and deceleration c_d curves occurs in the range M = 1.6 to M = 2.1, where the blue dashed line represents the c_d of the Busemann biplane airfoil during acceleration and the red solid line represents the c_d of the Busemann biplane airfoil during deceleration. This separation between the two c_d curves is caused by the flow-hysteresis phenomenon during acceleration and the choked-flow phenomenon during deceleration. Therefore, in order to minimize the difference in the drag coefficients of the Busemann biplane airfoil during acceleration and deceleration as well as to significantly decrease the drag, shape optimization of the baseline Busemann airfoil is conducted using single-objective genetic algorithm (SOGA) to eliminate the flow-hysteresis phenomenon during acceleration and the choked-flow phenomenon during deceleration; it is discussed in the next section.

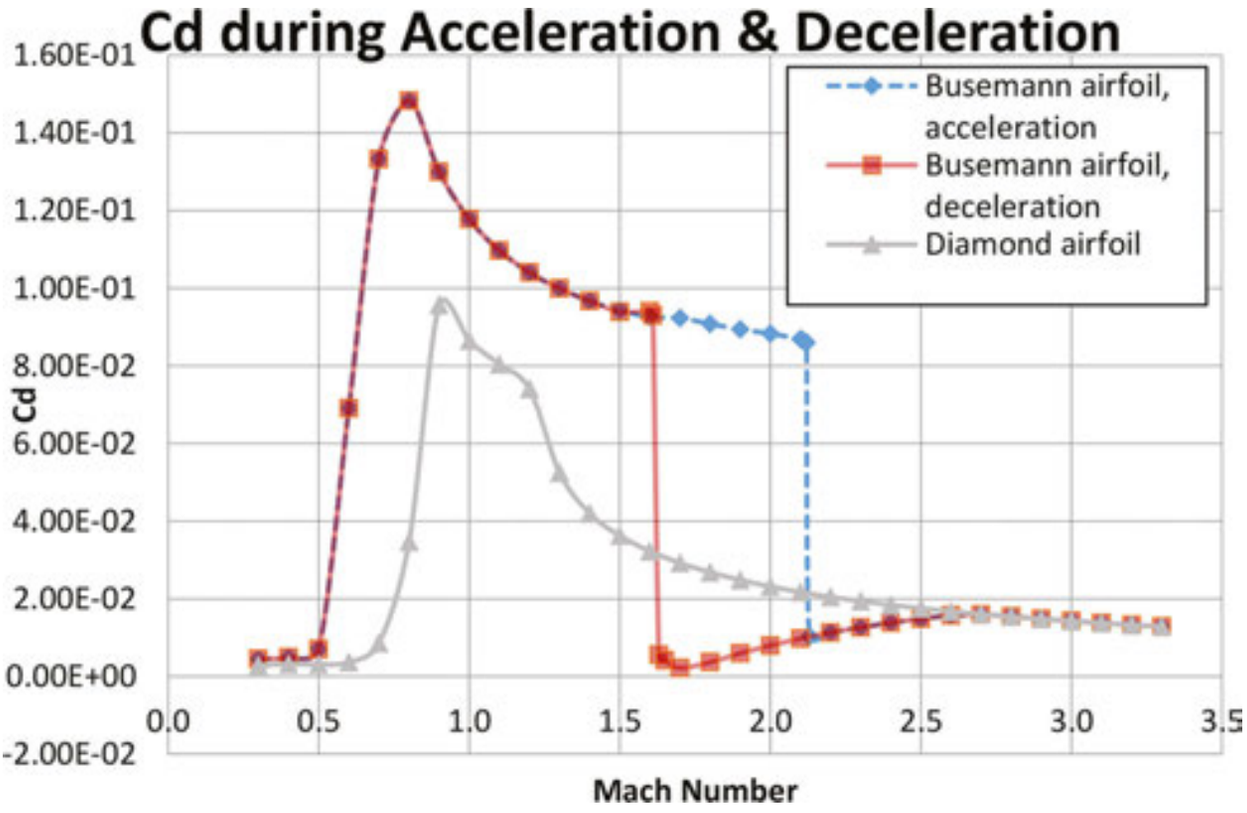

Figure 5. c_d plots for diamond-shaped airfoil and baseline Busemann airfoil during acceleration and deceleration under non-lifting conditions.

http://dx.doi.org/10.5772/62811

2.4. Flow field of the baseline Busemann biplane airfoil during acceleration

In this section, the flow-hysteresis phenomenon during acceleration is examined for the baseline Busemann biplane airfoil under the non-lifting condition. The pressure coefficient contours for flow past the baseline Busemann biplane airfoil during acceleration are shown in **Figure 6**. To simulate the non-lifting condition, the angle of attack is set to 0. The resulting non-lifting flow field around the baseline Busemann airfoil is shown in **Figure 6** at various supersonic Mach numbers ranging from M = 1.7 to M = 2.13. As shown in **Figure 6**, the bow shock exists in front of the Busemann airfoil and does not disappear until the Mach number reaches 2.13. It can also be noticed that there is a subsonic region behind the bow shock between the upper and lower components of the airfoil where the pressure coefficients are high. The presence of this bow shock in front of the airfoil results in a substantial increase in the drag compared to that at the design condition. However, when the Mach number increases from 2.12 to 2.13, the bow shock is swallowed into the upper and lower components of the Busemann airfoil and is replaced by two oblique shock waves, and the subsonic region between the two airfoil components finally disappears as shown in **Figure 6(d)**. The drag coefficient of the airfoil also decreases dramatically, and the flow past the airfoil develops into a state similar to that under the design condition. **Figure 6** illustrates the poor performance of the baseline Busemann airfoil under off-design conditions. During acceleration, the design condition cannot be achieved at Mach 1.7. And the drag coefficient at Mach 1.7 is much higher (c_d = 0.0923) compared to that of the standard diamond-shaped airfoil (c_d = 0.0292). Furthermore, due to the flow-hysteresis phenomenon, the drag coefficients c_d during acceleration and deceleration are different as shown in **Figure 6**.

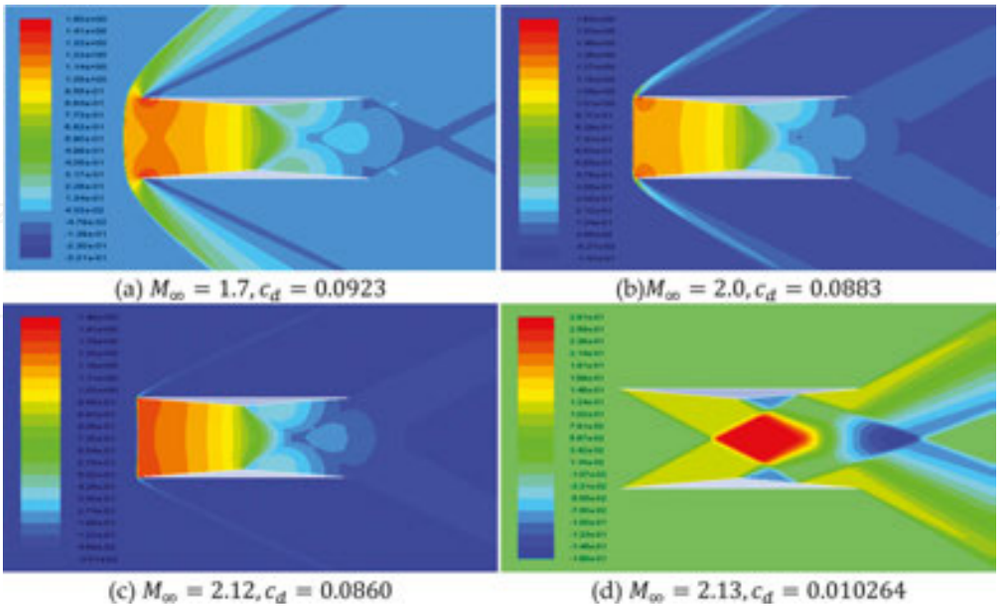

Figure 6. c_p-contours around the baseline Busemann biplane airfoil with zero lift during acceleration. (a) M_∞ = 1.7, c_d = 0.0923; (b) M_∞ = 2.0, c_d = 0.0883; (c) M_∞ = 2.12, c_d = 0.0860; (d) M_∞ = 2.13, c_d = 0.010264.

2.5. Flow field of the baseline Busemann biplane airfoil during deceleration

In this section, the choked-flow phenomenon of the baseline Busemann biplane airfoil during deceleration is examined. The contours of pressure coefficients for flow past the baseline Busemann airfoil during deceleration are shown in **Figure 7**. To simulate the non-lifting condition, the angle of attack is set to 0 as before. The resulting non-lifting flow field around the baseline Busemann airfoil is shown in **Figure 7** at various supersonic Mach numbers ranging from $M = 1.8$ to $M = 1.62$. As shown in **Figure 7**, a different flow field appears within the small range near the design Mach number ($M = 1.7$); a relatively high drag coefficient still occurs as the Mach number further decreases during deceleration. A strong bow shock is formed in front of the airfoil when the Mach number drops from 1.63 to 1.62, while the drag coefficient increases dramatically from 0.005594 to 0.0926, which is substantially higher than that of the standard diamond-shaped airfoil ($c_d = 0.03158$). The flow between the two components of the airfoil is choked at the location of the maximum thickness of the Busemann airfoil, and a subsonic region is formed. This is also a clear indication of the poor performance of the baseline Busemann biplane airfoil under off-design conditions as the drag coefficient of the baseline Busemann airfoil is much higher than that of the standard diamond-shaped airfoil for $M \leq 1.62$.

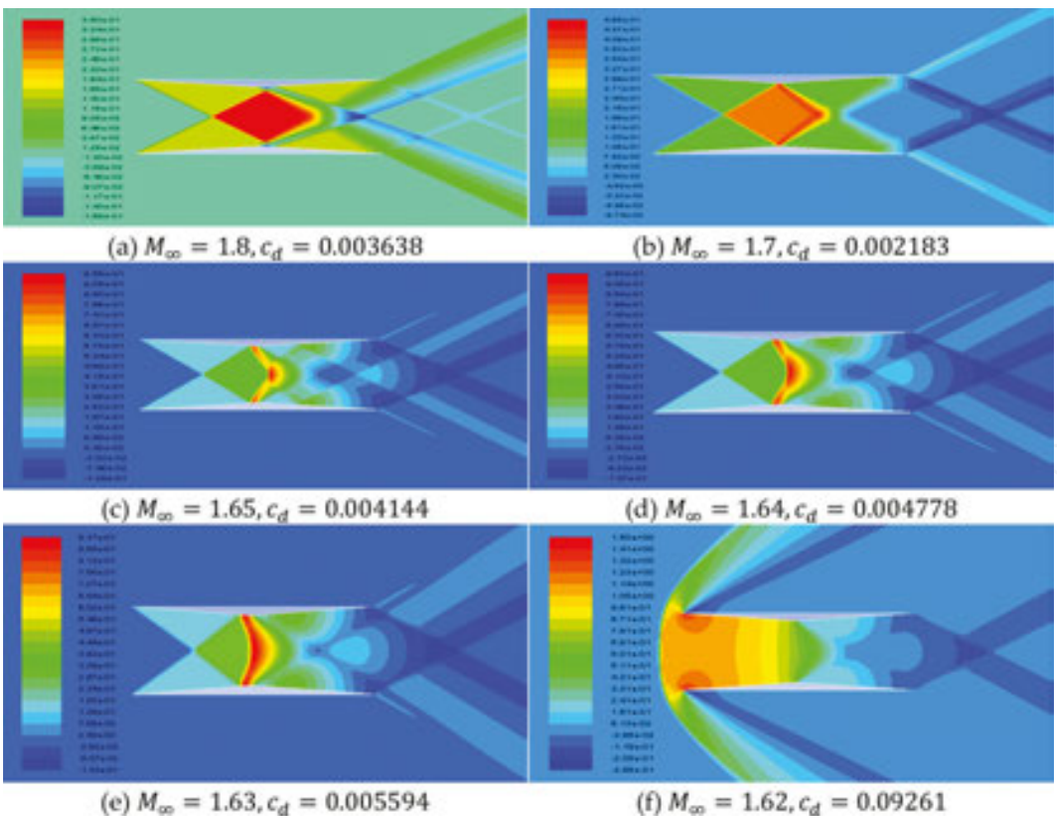

Figure 7. c_p-contours around the baseline Busemann biplane airfoil with zero lift during deceleration: (a) $M_\infty = 1.8$, $c_d = 0.003638$; (b) $M_\infty = 1.7$, $c_d = 0.002183$; (c) $M_\infty = 1.65$, $c_d = 0.004144$; (d) $M_\infty = 1.64$, $c_d = 0.004778$; (e) $M_\infty = 1.63$, $c_d = 0.005594$; (f) $M_\infty = 1.62$, $c_d = 0.09261$.

http://dx.doi.org/10.5772/62811

In conclusion, the baseline Busemann biplane airfoil produces a substantially higher drag in the low Mach number range (below the design Mach number of $M = 1.7$). Additionally, it is necessary to accelerate the baseline Busemann biplane airfoil to a much higher Mach number ($M = 2.13$) to reach the shock-wave-swallowing state, while dramatically producing higher drag and largely decreasing its efficiency, and then decelerate to a lower velocity to achieve the design condition at Mach number $M = 1.7$. As a result, the baseline Busemann biplane airfoil design needs to be modified and optimized to avoid or at least reduce the high drag coefficient caused by the flow-hysteresis phenomenon during acceleration and the choked-flow phenomenon during deceleration.

3. Optimization of Busemann-type biplane airfoil

In this chapter, the shape optimization procedure for the baseline Busemann biplane airfoil using the genetic algorithms (GAs) and the results of the optimized Busemann-type airfoil under both non-lifting and lifting conditions are presented. The optimization process is established by coupling a single-objective genetic algorithm (SOGA)- or a multi-objective genetic algorithm (MOGA)-based optimization method with the mesh generation software ANSYS-ICEM and the CFD solver ANSYS FLUENT as shown in **Figure 8**.

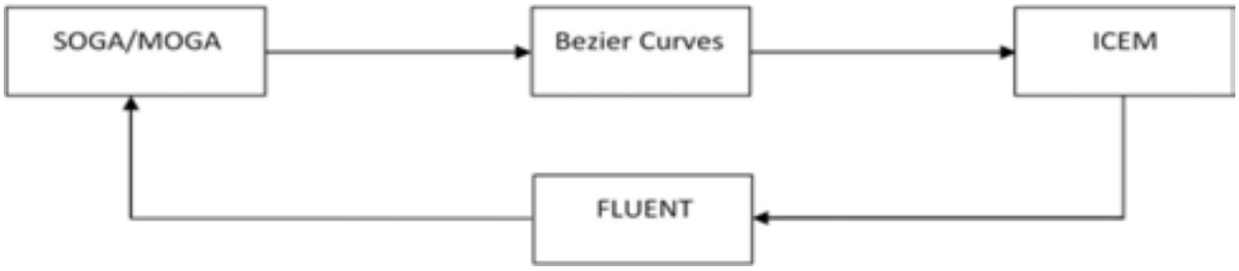

Figure 8. Schematic of information flow in the optimization process.

Every individual (airfoil) in each generation of SOGA/MOGA is represented by a set of control points, which randomly generate the airfoil shape by using the Bezier curves. The mesh generation software ICEM is used to generate a two-dimensional structured mesh around the airfoil as an input to the CFD solver FLUENT, which is then used to calculate the supersonic inviscid flow fields for specific flow conditions. Based on the fitness values of all airfoil shapes in a given generation, SOGA/MOGA is applied to create the next generation of airfoils, and this whole process is repeated until the optimal fitness value is obtained. The airfoil shape that corresponds to the optimal fitness value is the final shape of the optimized airfoil [18].

3.1. Overview of genetic algorithm

Genetic algorithms (GAs) are a class of stochastic optimization algorithms inspired by the biological evolution [19]. They efficiently exploit historical information to speculate on new offspring with improved performance [20]. For the Busemann biplane airfoil in particular,

genetic algorithms are used to generate new shapes that produce much lower drag by minimizing the flow-hysteresis phenomenon during acceleration and the choked-flow phenomenon during deceleration. Generally, The GA employs the following steps to complete the optimization process:

1. Initialization: randomly generates a group of individuals.
2. Evaluation: evaluates the fitness of each individual generated.
3. Natural selection: individuals who have the lowest fitness are removed.
4. Reproduction: pairs of individuals are picked to produce the offspring, which is often done by roulette wheel sampling. A crossover function is then used to produce the offspring.
5. Mutation: randomly modifies some small percentage of the population.
6. Check for convergence: if the current generation has converged, the individual having the best fitness will be returned. Otherwise, the process will be repeated starting from Step 2 until the predefined tolerance criteria for acceptable change in fitness between generations are met.

3.1.1. Application of single-objective genetic algorithm (SOGA)

For the non-lifting condition, when the lift coefficient $c_l = 0$, a single-objective genetic algorithm (SOGA) is employed for the shape optimization of the Busemann biplane airfoil. The single objective to be achieved is to minimize the drag coefficient c_d. Multiple design points (Mach numbers) are used during the optimization process due to the flow-hysteresis and choked-flow phenomena caused by the baseline Busemann biplane airfoil during acceleration and deceleration, respectively. For the multi-point optimization, the fitness function employed is a weighted average of the drag coefficients c_d, which can be written in the following form:

$$I = \frac{\sum_{i=1}^{n} w_i I_i}{\sum_{i=1}^{n} w_i} \tag{1}$$

where I is the weighted average drag coefficient, and "i" denotes a design point (related to Mach number). For the optimization process under the non-lifting condition, an evenly weighted average of drag coefficients c_d at different Mach numbers is employed. Therefore, Eq. (1) reduces to

$$I = \frac{\sum_{i=1}^{n} I_i}{n} \tag{2}$$

As the wave drag of the Busemann biplane airfoil is much lower when the flow is unchoked, it is highly desirable that the strong bow shock wave in front of the airfoil is swallowed into

http://dx.doi.org/10.5772/62811

the area between the upper and lower components of the airfoil before the flow speed approaches the design Mach number (M = 1.7). Although a higher weight can be assigned to the most important design Mach number (M = 1.7) to produce a lower drag at that design point, previous research conducted by Hu et al. [17] has shown that a slightly higher drag coefficient c_d is obtained at lower Mach numbers during acceleration and deceleration, as given in **Tables 1** and **2**, respectively, if such an uneven weighting method is used.

Mach number	**1.1**	**1.2**	**1.3**	**1.4**	**1.5**	**1.6**	**1.7**
Baseline	1050	996	957	928	906	889	873
Optimized (even)	527	473	419	376	332	112	106
Optimized (uneven)	539	486	428	382	336	107	101

Table 1. Comparison of c_d at under zero-lift conditions during acceleration (1 count = 0.0001) [17].

Mach number	**1.7**	**1.6**	**1.5**	**1.4**	**1.3**	**1.2**	**1.1**
Baseline	873	889	906	928	957	996	1050
Optimized (even)	106	112	127	152	419	473	527
Optimized (uneven)	101	107	122	146	428	486	539

Table 2. Comparison of c_d at under zero-lift conditions during deceleration (1 count = 0.0001) [17].

GA parameters	**Description**
Generation size	8 individuals per generation
Number of generations	Maximum of 50 generations if convergence not obtained
Number of design variables	14 in total, 7 for acceleration and 7 for deceleration
Selection type	Roulette Wheel Selection
Crossover rate	0.7
Mutation rate	0.1
Error of mutation constant	0.8, which determines how much mutation affects the curves as generations proceed

Table 3. GA parameters for shape optimization of Busemann biplane airfoil under non-lifting conditions.

Here, we have a total of seven design points in the Mach numbers ranging from M = 1.1 to M = 1.7, for both acceleration and deceleration. The reason for picking these seven design points is that this range of Mach numbers, M = 1.1 to M = 1.7, provides the critical region before the Mach number increases to the design condition M = 1.7; it is the region in which we want to maintain the drag coefficient as low as possible. Both acceleration and deceleration scenarios are considered in order to reduce the flow-hysteresis phenomenon and the choked-flow phenomenon, respectively.

A code in the MATLAB package is developed and utilized in the optimization process of the airfoil as well as for ICEM meshing and FLUENT flow field calculations. All SOGA parameters are defined based on the GA methodology, as shown in **Table 3**.

3.1.2. Airfoil parameterization

The shape of the airfoil is generated by using the Bezier curves (third-order polynomials). Bezier curves are frequently used in computer graphics to obtain curves that appear to be reasonably smooth at all scales. One of the main reasons that Bezier curves are used in computer graphics is that they can be efficiently constructed; each Bezier curve is simply defined by a set of control points [21].

For the non-lifting case, with $c_l = 0$, since the upper and lower components of the airfoil are symmetric with respect to the horizontal axis, only the upper component of the airfoil needs to be defined; the lower component is the mirror image with respect to the horizontal axis. For the upper component of the airfoil, there are two lines that need to be drawn to define its shape. Since the thickness distribution for the entire airfoil remains the same as that of the baseline Busemann biplane airfoil, the y-coordinates of the lower line are defined by Eqs. (3) and (4). Thus, the upper line (which is a straight horizontal line for the baseline Busemann airfoil) is the only line that needs to be generated by the Bezier curves in order to define the shape of the whole biplane airfoil.

$$y_{low} = y_{up} - 0.05 - 0.1 \times x_{up} (-0.5 \le x_{up} \le 0) \tag{3}$$

$$y_{low} = y_{up} - 0.05 + 0.1 \times x_{up} (0 \le x_{up} \le 0.5) \tag{4}$$

In Eqs. (3) and (4), the subscripts "low" and "up" correspond to the lower and upper lines of the airfoil; the origin is at the center of the upper line. Two Bezier curves are used to generate the shape-defining upper line. Each Bezier curve is defined by a set of four control points. Each control point is constrained by a specified range of x- and y-coordinates. **Figure 9** shows a randomly generated Busemann-type biplane airfoil shape using Bezier curves.

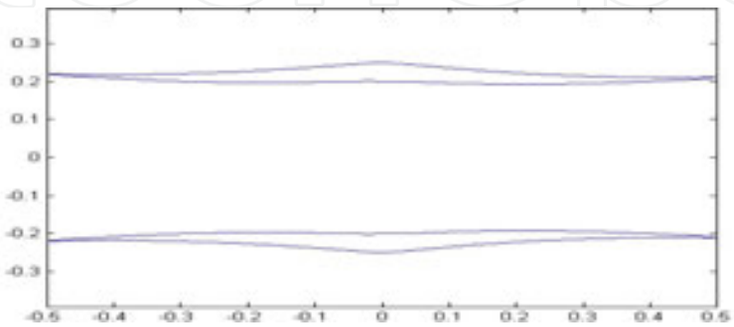

Figure 9. Randomly generated Busemann-type biplane airfoil shape using Bezier curves.

http://dx.doi.org/10.5772/62811

3.1.3. Optimization results

After implementing SOGA for 20 generations with eight individuals in each generation, an optimal shape result for symmetric Busemann-type biplane airfoil under the non-lifting condition with a minimum drag is obtained. **Figure 10** shows the geometry of the original Busemann biplane airfoil (red) and the optimized Busemann biplane airfoil (blue) under the non-lifting condition.

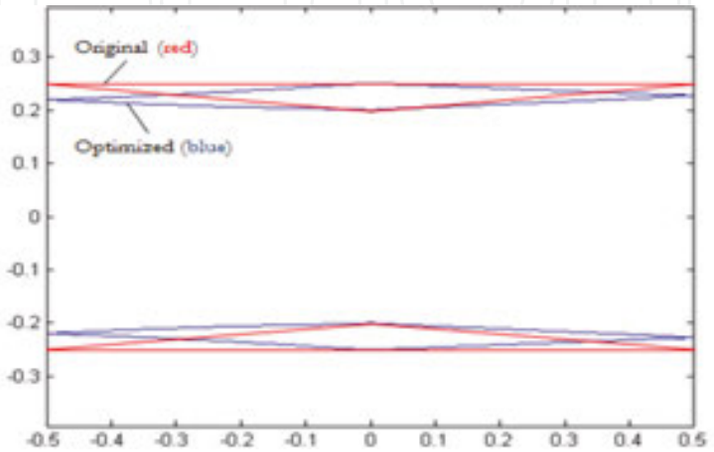

Figure 10. Geometry of both the original and optimized Busemann biplane airfoil under non-lifting conditions.

Mach number	**1.1**	**1.2**	**1.3**	**1.4**	**1.5**	**1.6**	**1.7**
Baseline	1097	1040	999	967	943	926	923
Optimized (GA)	622	506	428	389	132	114	104

Table 4. Comparison of c_d for the original and optimized Busemann biplane airfoil under non-lifting conditions during acceleration (1 count = 0.0001).

Mach number	**1.7**	**1.6**	**1.5**	**1.4**	**1.3**	**1.2**	**1.1**
Baseline	32	926	940	967	999	1040	1098
Optimized (GA)	104	114	132	163	428	506	621

Table 5. Comparison of c_d for the original and optimized Busemann biplane airfoil under non-lifting conditions during deceleration (1 count = 0.0001).

The drag coefficients for the seven design points are compared in **Tables 4** and **5** for both the original and optimized Busemann biplane airfoil under the non-lifting condition during acceleration and deceleration, respectively. As shown in **Tables 4** and **5**, the baseline Busemann biplane airfoil is choked at all Mach numbers within the optimization range, while the optimized Busemann biplane airfoil un-chokes at M = 1.5 during acceleration and chokes at M = 1.3 during deceleration. Even under choked conditions during both acceleration and

deceleration, the optimized Busemann biplane airfoil has significantly lower drag compared to the baseline Busemann biplane airfoil. The only point where the optimized Busemann biplane airfoil has a higher drag compared to the original airfoil is at $M = 1.7$ during deceleration.

Figures 11 and **12**, respectively, show the change in the pressure coefficient c_p around the original Busemann biplane airfoil as the Mach number increases and decreases within the design-point range. The corresponding c_p contours for the optimized Busemann biplane airfoil are shown in **Figures 13** and **14** to illustrate the wave-cancellation effect.

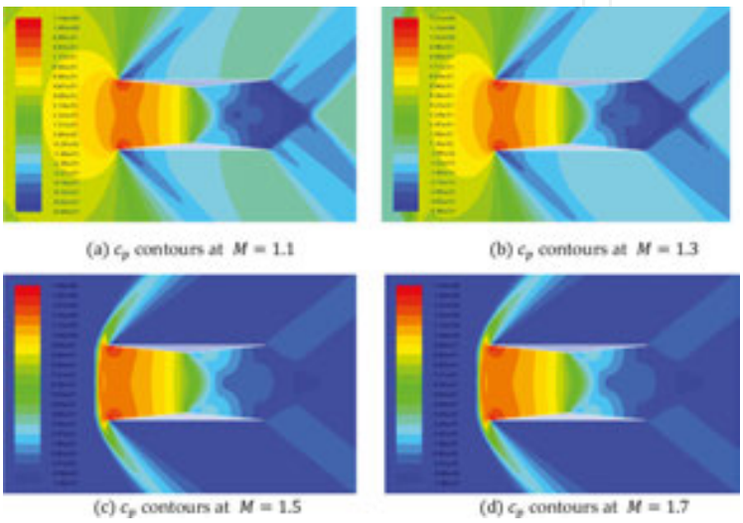

Figure 11. c_p contours around the original Busemann biplane airfoil during acceleration: (a) c_p contours at $M = 1.1$; (b) c_p contours at $M = 1.3$; (c) c_p contours at $M = 1.5$; (d) c_p contours at $M = 1.7$.

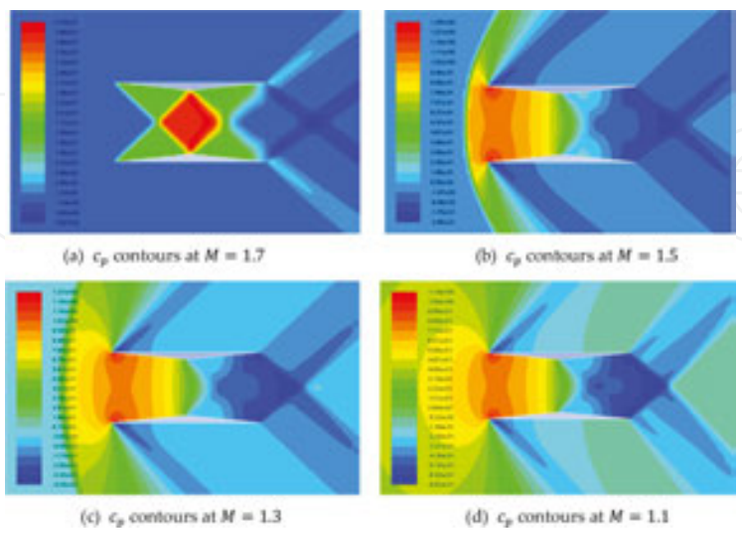

Figure 12. c_p contours around the original Busemann biplane airfoil during deceleration: (a) c_p contours at $M = 1.7$; (b) c_p contours at $M = 1.5$; (c) c_p contours at $M = 1.3$; (d) c_p contours at $M = 1.1$.

http://dx.doi.org/10.5772/62811

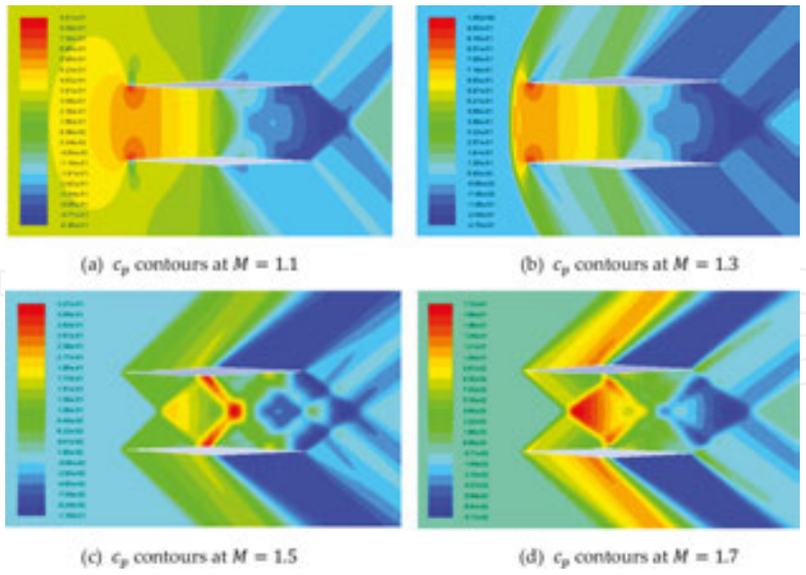

Figure 13. c_p contours around the optimized Busemann biplane airfoil during acceleration: (a) c_p contours at $M = 1.1$; (b) c_p contours at $M = 1.3$; (c) c_p contours at $M = 1.5$; (d) c_p contours at $M = 1.7$.

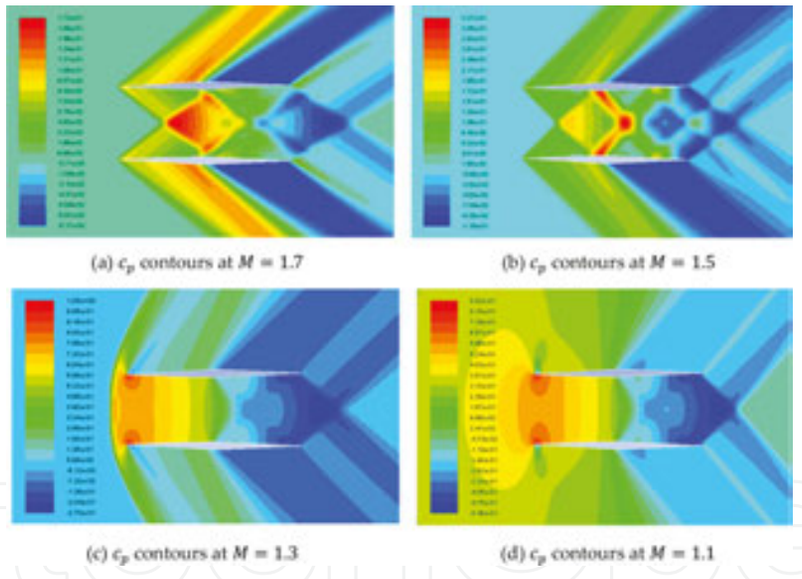

Figure 14. c_p contours around the optimized Busemann biplane airfoil during deceleration: (a) c_p contours at $M = 1.7$; (b) c_p contours at $M = 1.5$; (c) c_p contours at $M = 1.3$; (d) c_p contours at $M = 1.1$.

Figure 15 shows the comparison of the drag coefficients for the standard diamond-shaped airfoil, the baseline Busemann biplane airfoil, and the optimized Busemann biplane airfoil under the non-lifting condition. As shown in this figure, the separation between the acceleration and deceleration curves for c_d still exists for the optimized Busemann biplane airfoil, which means that the flow-hysteresis and the choked-flow effects are not totally eliminated. However, as clearly shown in **Figure 15**, the flow-hysteresis area has been significantly reduced, and the drag increase during deceleration due to the choked-flow phenomenon is much

smaller than that for the original Busemann biplane airfoil. The drag of the optimized Busemann biplane airfoil in the subsonic region is also smaller than that of the original Busemann biplane airfoil, although it is slightly higher than that of the standard diamond-shaped airfoil with $0.6 < M < 0.85$. Under both subsonic and supersonic conditions, the optimized Busemann biplane airfoil has been able to significantly reduce the wave drag compared to the original Busemann biplane airfoil. At the design condition Mach number of 1.7, however, the drag coefficient of the optimized Busemann biplane airfoil ($c_d = 0.01038$) is much higher than that of the original Busemann biplane airfoil $c_d = 0.002182$. This is due to the fact that for the shape optimization, our focus has been on reducing the flow-hysteresis and choked-flow effects, and we chose to assign equal weights to all Mach numbers used as the multiple design points. To address this problem, we could have put more weight on the design condition ($M = 1.7$) during the optimization process.

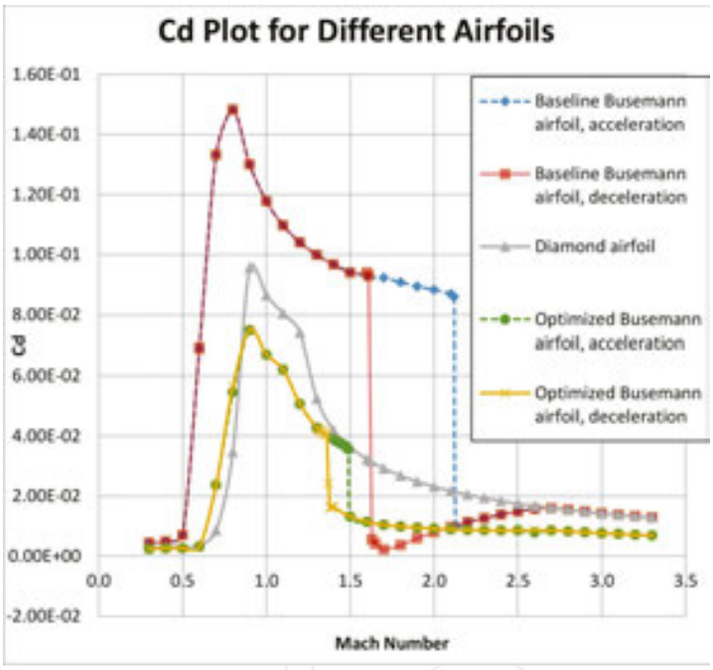

Figure 15. c_d plot for different airfoils under nonlifting condition.

Next, we examine the details of the flow field during acceleration and deceleration for the optimized Busemann biplane airfoil and compare them with the original baseline Busemann biplane airfoil and the optimization results obtained by Hu et al. [17] using an adjoint-based optimization technique. **Figures 16** and **17** show the pressure coefficient contours of the optimized Busemann biplane airfoil under acceleration and deceleration, respectively. **Figures 18** and **19** show the pressure coefficient contours of the optimized Busemann biplane airfoil using the adjoint-based technique [17] under acceleration and deceleration, respectively. During acceleration, the flow-hysteresis effect still exists, and a bow shock wave is formed in front of the airfoil. The swallowing of the bow shock wave happens when the Mach number increases from 1.49 to 1.50 in our GA optimization as shown in **Figure 16(f)**; it happens when the Mach number increases from 1.52 to 1.53 in the adjoint-based optimization as shown in

http://dx.doi.org/10.5772/62811

Figure 18(e), and it happens when the Mach number increases from 2.12 to 2.13 for the original Busemann biplane airfoil as shown in **Figure 6(d)**. The drag coefficient decreases from 0.03556 to 0.01316 in the present GA-based optimization and from 0.03336 to 0.01221 in the adjoint-based optimization [17].

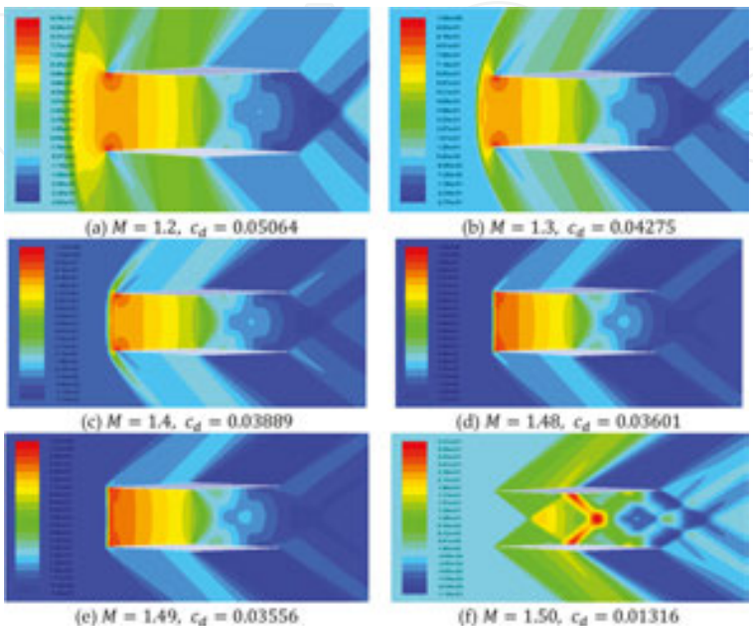

Figure 16. c_p contours of the GA-optimized Busemann biplane airfoil with zero lift during acceleration: (a) $M = 1.2$, $c_d = 0.05064$; (b) $M = 1.3$, $c_d = 0.04275$; (c) $M = 1.4$, $c_d = 0.03889$; (d) $M = 1.48$, $c_d = 0.03601$; (e) $M = 1.49$, $c_d = 0.03556$; (f) $M = 1.50$, $c_d = 0.01316$.

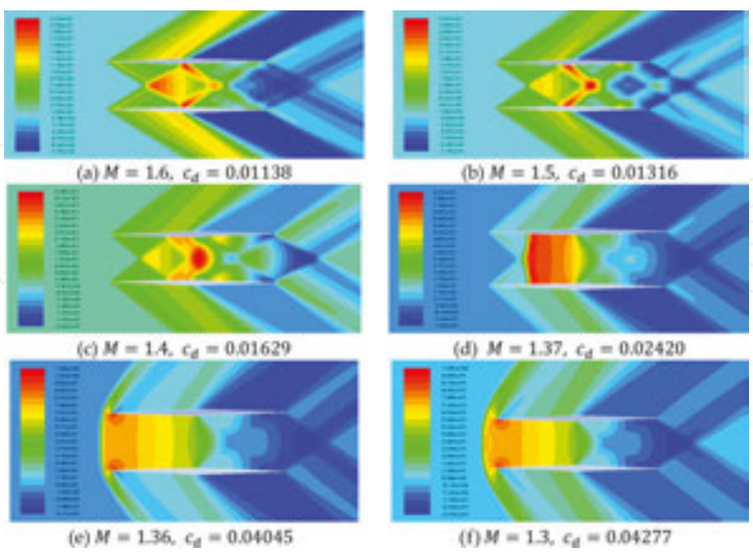

Figure 17. c_p contours of the GA-optimized Busemann biplane airfoil with zero lift during deceleration: (a) $M = 1.6$, $c_d = 0.01138$; (b) $M = 1.5$, $c_d = 0.01316$; (c) $M = 1.4$, $c_d = 0.01629$; (d) $M = 1.37$, $c_d = 0.02420$; (e) $M = 1.36$, $c_d = 0.04045$; (f) $M = 1.3$, $c_d = 0.04277$.

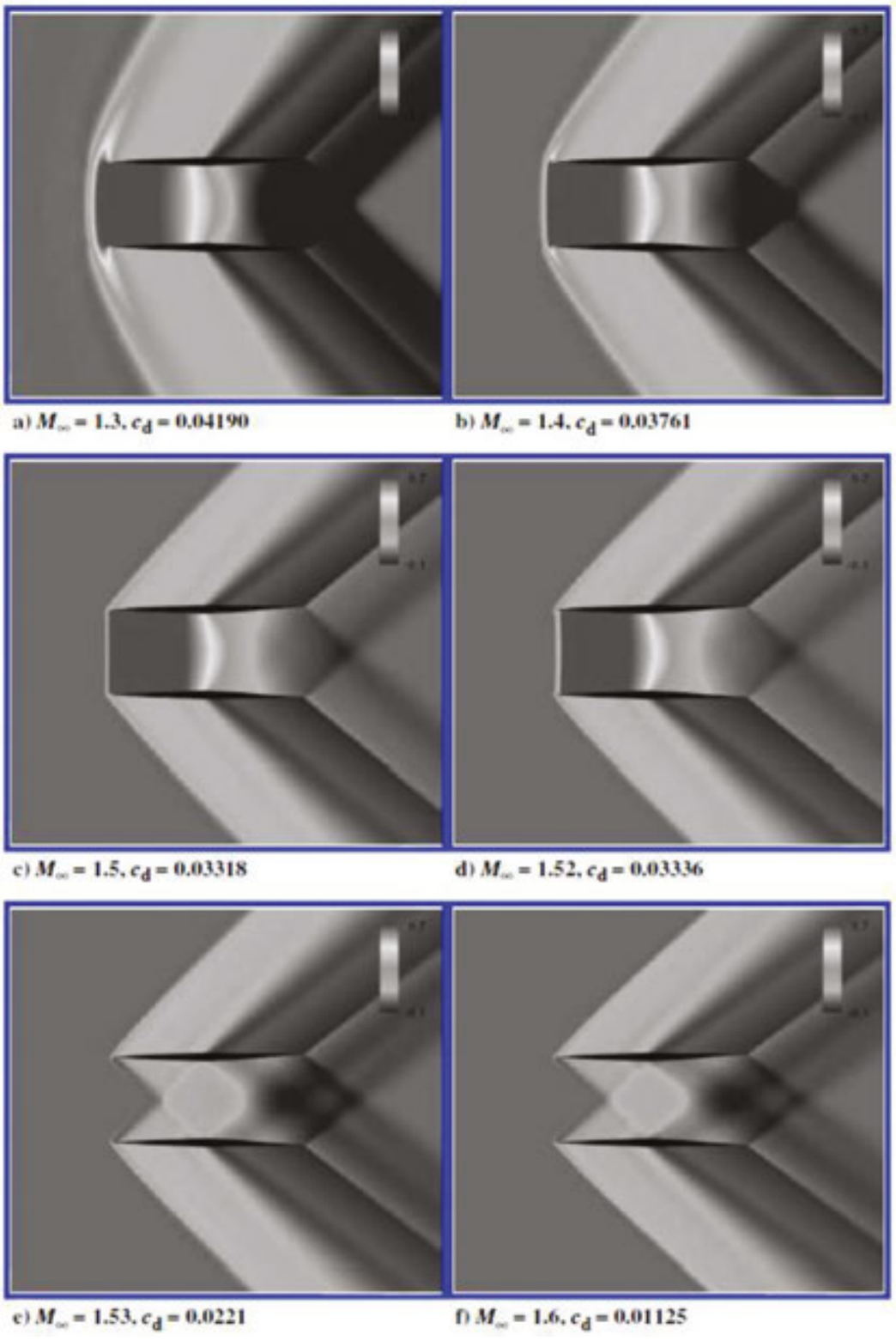

Figure 18. c_p contours of the adjoint-based-optimized Busemann biplane airfoil with zero lift during acceleration [17]: (a) $M_\infty = 1.3$, $c_d = 0.04190$; (b) $M_\infty = 1.4$, $c_d = 0.03761$; (c) $M_\infty = 1.5$, $c_d = 0.03318$; (d) $M_\infty = 1.52$, $c_d = 0.03336$; (e) $M_\infty = 1.53$, $c_d = 0.0221$; (f) $M_\infty = 1.6$, $c_d = 0.01125$.

http://dx.doi.org/10.5772/62811

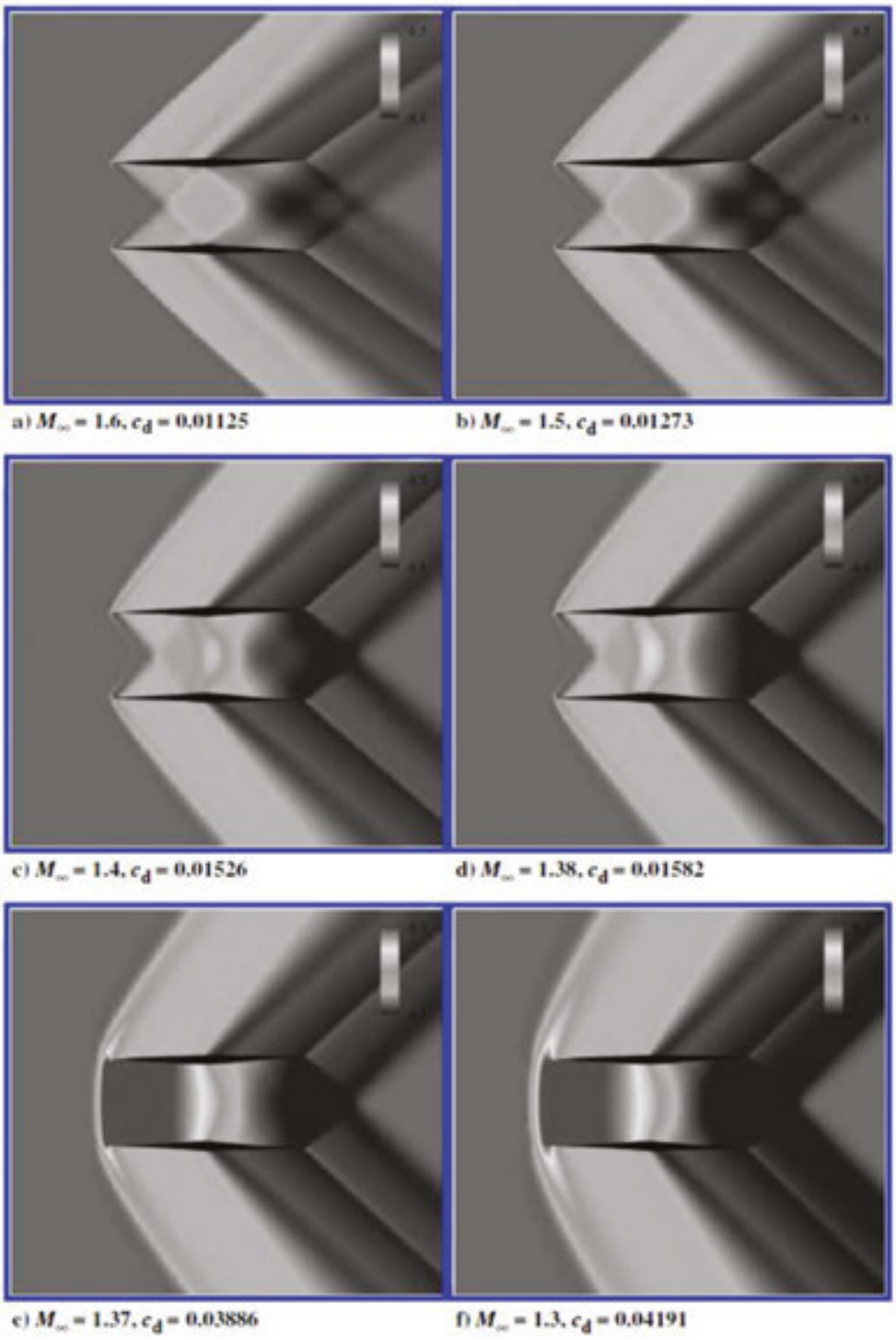

Figure 19. c_p contours of the adjoint-based-optimized Busemann biplane airfoil with zero lift during deceleration [17]: (a) $M_\infty = 1.6$, $c_d = 0.01125$; (b) $M_\infty = 1.5$, $c_d = 0.01273$; (c) $M_\infty = 1.4$, $c_d = 0.01526$; (d) $M_\infty = 1.38$, = 0.01582; (e) $M_\infty = 1.37$, $c_d = 0.03886$; (f) $M_\infty = 1.3$, $c_d = 0.04191$.

In conclusion, as shown in **Figure 20**, the drag coefficient of the GA-optimized Busemann biplane airfoil is significantly reduced when compared to the original Busemann biplane airfoil, and it matches with the adjoint-based optimization result obtained by Hu et al. [17].

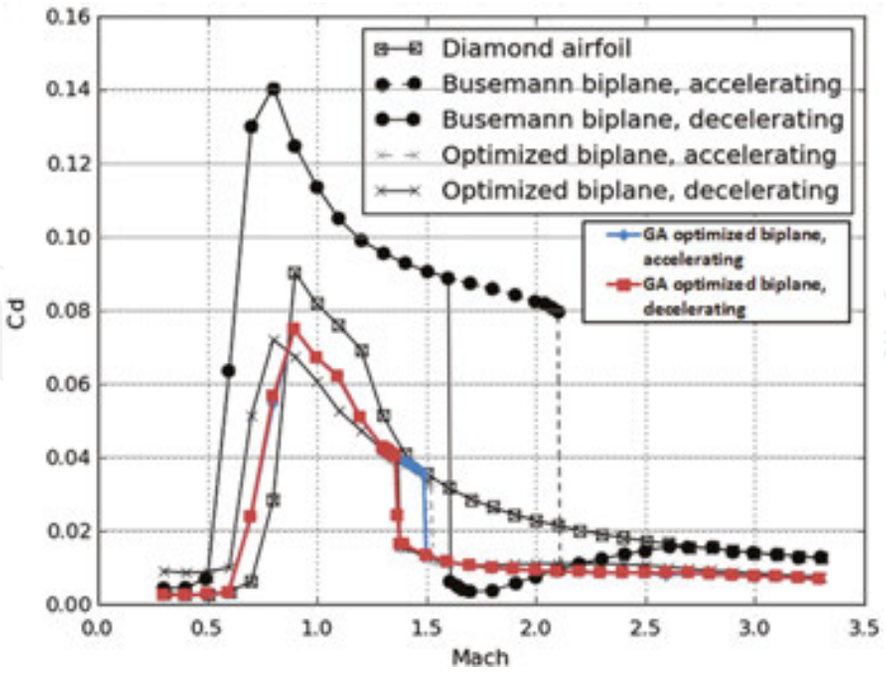

Figure 20. c_d plot for different airfoils under non-lifting conditions.

3.2. Shape optimization of Busemann biplane airfoil under lifting conditions

3.2.1. Application of multi-objective genetic algorithm (MOGA)

Under the lifting condition with the lift coefficient $c_l \neq 0$, a multi-objective genetic algorithm (MOGA) is employed for shape optimization of the original Busemann biplane airfoil. The two objectives to be achieved are to minimize the drag coefficient c_d while maximizing the lift coefficient c_l. Similar to that for the non-lifting condition described in Section 3.2, a total of seven design points ranging from $M = 1.1$ to $M = 1.7$ are used during the optimization process. For the fitness functions for the lifting case, we use the sum of evenly weighted average of both c_d and c_l. The GA parameters used for the lifting case are listed in **Table 6**.

GA parameters	Description
Generation size	8 individuals per generation
Number of generations	Maximum of 50 generations if convergence not obtained
Number of design variables	28 in total, 14 (7 for c_d & 7 for c_l) for acceleration and 14 (7 for c_d & 7 for c_l) for deceleration
Selection type	Roulette Wheel Selection
Crossover rate	0.7
Mutation rate	0.1
Error of mutation constant	0.8, which determines how much mutation affects the curves as generations go on

Table 6. GA parameters for shape optimization of Busemann biplane airfoil under lifting conditions.

http://dx.doi.org/10.5772/62811

3.2.2. Airfoil parameterization

Similar to that for the non-lifting case, the random shapes of the airfoil are generated by using the Bezier curves with control points. For the lifting case with $c_l \neq 0$, as the upper and lower components of the biplane airfoil are not symmetric, both the upper and lower components need to be defined separately. The thickness distribution for both the upper and lower components is still maintained the same as for the non-lifting case. Now, a total of four Bezier curves are needed to define the shape of the airfoil. **Figure 21** shows a randomly generated Busemann-type biplane airfoil shape using the Bezier curves for lifting conditions.

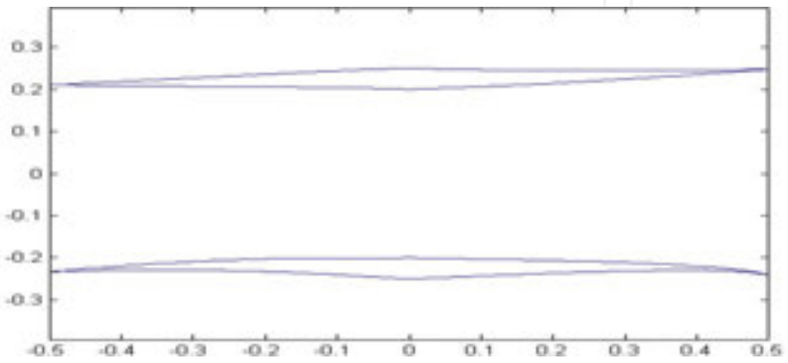

Figure 21. Randomly generated Busemann-type biplane airfoil shape using the Bezier curves for lifting conditions.

3.2.3. Optimization results

After implementing MOGA for 20 generations with eight individuals in each generation, an optimal shape for asymmetric Busemann-type airfoil under lifting conditions with maximum c_l and minimum c_d is obtained. **Figure 22** shows the geometry of the original Busemann biplane airfoil (red) and the optimized Busemann biplane airfoil (blue) under lifting conditions.

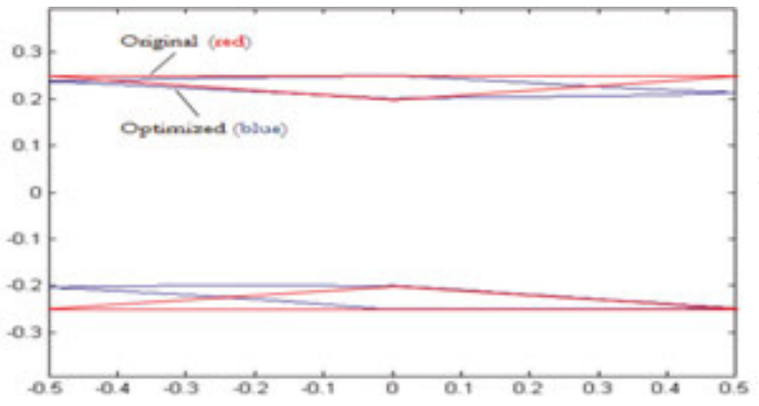

Figure 22. Geometry of both the original and optimized Busemann biplane airfoil under lifting condition.

The drag coefficients for the seven design points are compared in **Tables 7** and **8** for both the original and optimized Busemann biplane airfoil under lifting condition. As shown in

Tables 7 and **8**, the baseline Busemann biplane airfoil is choked at all Mach numbers within the optimization range, while the optimized Busemann biplane airfoil is unchoked at M = 1.6 during acceleration and is choked at M = 1.3 during deceleration. Even under choked conditions during both acceleration and deceleration, the optimized Busemann biplane airfoil has significantly lower drag compared to the baseline Busemann biplane airfoil. Similar to the non-lifting condition, the only point where the optimized Busemann biplane airfoil has a higher drag compared to the original airfoil is at M = 1.7 during deceleration.

Mach number	**1.1**	**1.2**	**1.3**	**1.4**	**1.5**	**1.6**	**1.7**
Baseline	1097	1040	999	967	943	926	923
Optimized	683	633	529	461	418	148	136

Table 7. Comparison of c_d for the original and optimized Busemann biplane airfoil under lifting conditions during acceleration (1 count = 0.0001).

Mach number	**1.7**	**1.6**	**1.5**	**1.4**	**1.3**	**1.2**	**1.1**
Baseline	32	926	940	967	999	1040	1098
Optimized	136	148	173	224	529	633	682

Table 8. Comparison of c_d for the original and optimized Busemann biplane airfoil under lifting conditions during deceleration (1 count = 0.0001).

Figures 23 and **24** show a change in the pressure coefficient c_p around the optimized Busemann biplane airfoil under lifting condition as the Mach number increases and decreases within the design-point range. As can be seen from these figures, the bow shock wave in front of the airfoil disappears at M = 1.6 during acceleration and is not generated until the flow speed drops down to M = 1.3 during deceleration.

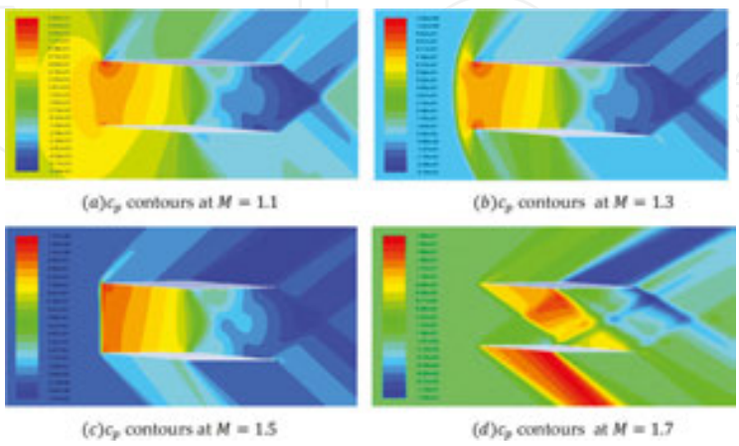

Figure 23. c_p contours for the optimized Busemann biplane airfoil under lifting conditions during acceleration: (a) c_p contours at M = 1.1; (b) c_p contours at M = 1.3; (c) c_p contours at M = 1.5; (d) c_p contours at M = 1.7.

http://dx.doi.org/10.5772/62811

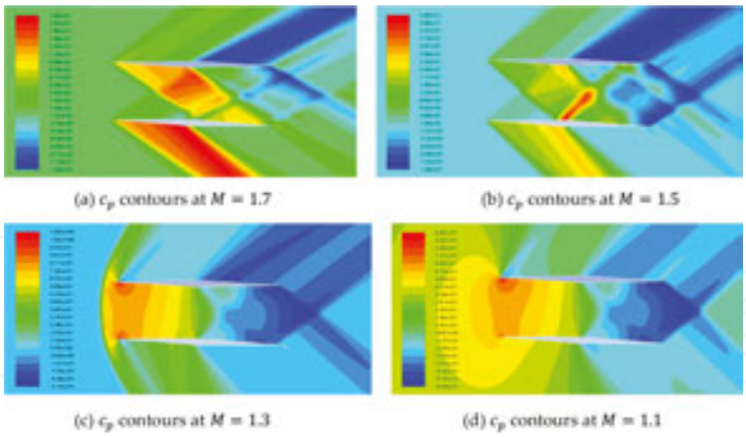

Figure 24. c_p contours for the optimized Busemann biplane airfoil under lifting condition during deceleration: (a) c_p contours at $M = 1.7$; (b) c_p contours at $M = 1.5$; (c) c_d contours at $M = 1.3$; (d) c_d contours at $M = 1.1$.

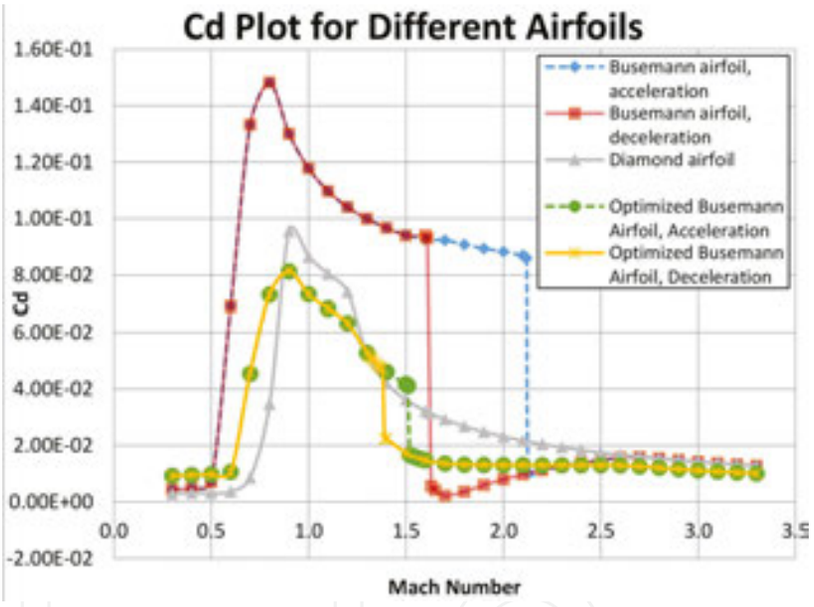

Figure 25. c_d plot for different airfoils under lifting conditions.

Figure 25 shows the comparison of the drag coefficients for the standard diamond-shaped airfoil, the baseline Busemann biplane airfoil and the optimized Busemann biplane airfoil under lifting condition. As shown in the figure, the separation between the acceleration and deceleration c_d lines still exists for the optimized Busemann biplane airfoil, which means that the flow-hysteresis and the choked-flow effects are not totally eliminated. However, as clearly shown in **Figure 25**, the flow-hysteresis area has been significantly reduced, and the drag increase during deceleration due to the choked-flow phenomenon is much smaller than that for the original Busemann biplane airfoil. The drag of the optimized Busemann biplane airfoil in the subsonic region is smaller than that of the original Busemann biplane airfoil, although it is slightly higher than that of the standard diamond-shaped airfoil with $0.3 < M < 0.85$. Under

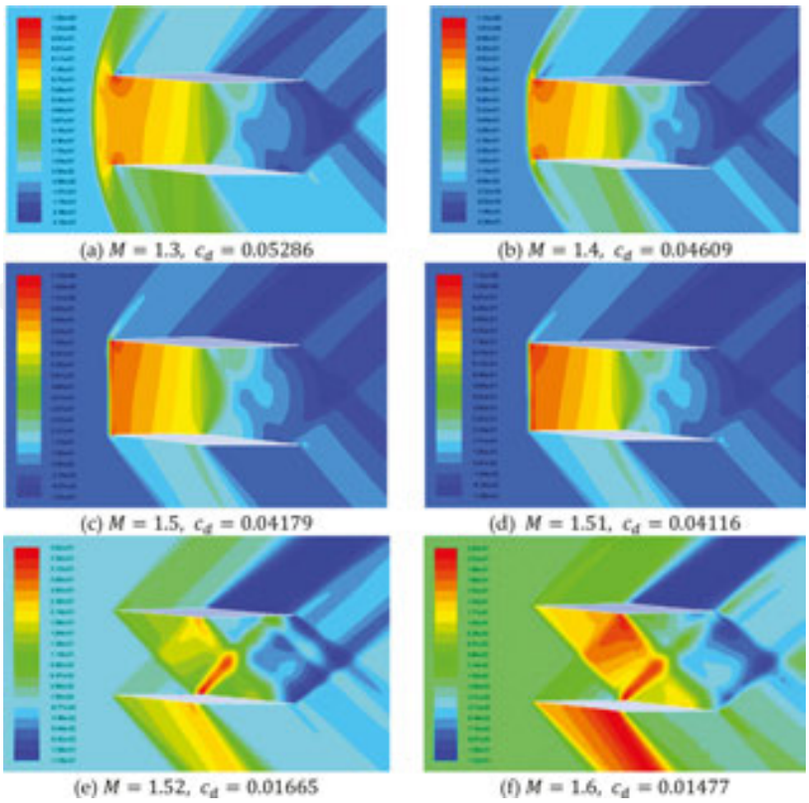

Figure 26. c_p contours of the GA-optimized Busemann biplane airfoil with lift during acceleration: (a) M = 1.3, c_d = 0.05286; (b) M = 1.4, c_d = 0.04609; (c) M = 1.5, c_d = 0.04179; (d) M = 1.51, c_d = 0.04116; (e) M = 1.52, c_d = 0.01665; (f) M = 1.6, c_d = 0.01477.

both subsonic and supersonic conditions, the optimized Busemann biplane airfoil has significantly reduced the wave drag compared to the original Busemann biplane airfoil. Similar to the non-lifting condition, the drag coefficient of the optimized Busemann biplane airfoil at M = 1.7 (c_d = 0.01362) is higher than that of the original Busemann biplane airfoil (c_d = 0.002182).

Next, we examine the details of the flow field during acceleration and deceleration for the optimized Busemann biplane airfoil under lifting conditions and compare them with the flow field of the original Busemann biplane airfoil. **Figures 26** and **27** show the pressure coefficient contours of the optimized Busemann biplane airfoil using GA during acceleration and deceleration, respectively. During acceleration, the flow-hysteresis effect still exists, and a bow shock wave is formed in front of the airfoil. The swallowing of the bow shock wave happens when the Mach number increases from 1.49 to 1.50 as shown in **Figure 16(f)** and from 2.12 to 2.13 for the original Busemann biplane airfoil as shown in **Figure 6(d)**. The corresponding drag coefficient decreases from 0.04116 to 0.01665 for the optimized Busemann biplane airfoil.

During deceleration, the choked-flow effect still exists; however, it is shifted to a lower Mach number of 1.38 compared to 1.6 for the original Busemann biplane airfoil.

In conclusion, the drag coefficient of the optimized Busemann biplane airfoil under lifting conditions is significantly reduced compared to the original Busemann biplane airfoil as shown

http://dx.doi.org/10.5772/62811

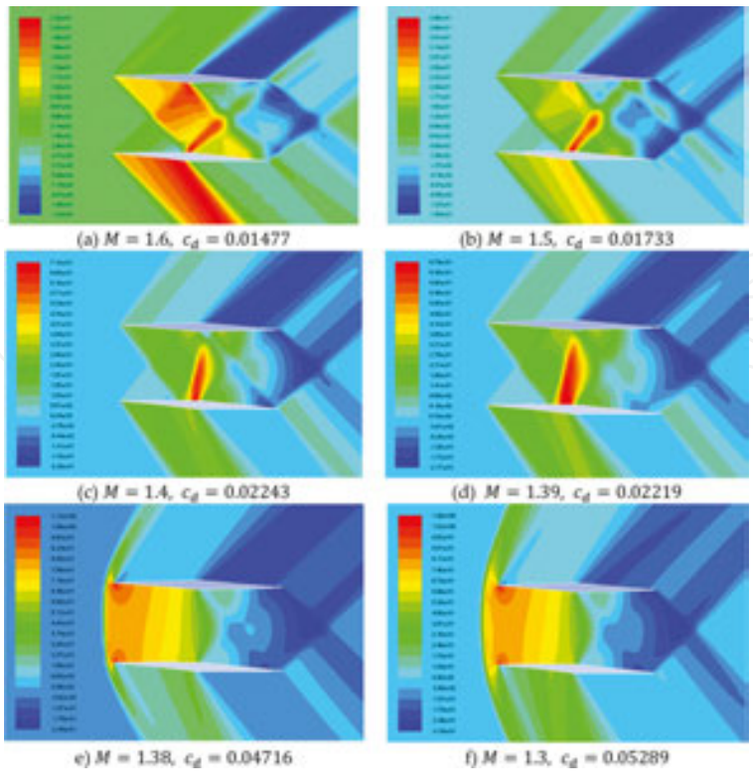

Figure 27. c_p contours of the GA-optimized Busemann biplane airfoil with lift during deceleration: (a) M = 1.6, c_d = 0.01477; (b) M = 1.5, c_d = 0.01733; (c) M = 1.4, c_d = 0.02243; (d) M = 1.39, c_d = 0.02219; (e) M = 1.38, c_d = 0.04716; (f) M = 1.3, = 0.05289.

in **Figures 25–27**. **Table 9** gives the lift coefficient of the optimized Busemann airfoil under lifting conditions at different design points.

Mach number	**1.1**	**1.2**	**1.3**	**1.4**	**1.5**	**1.6**	**1.7**
c_l (acceleration)	0.3319	0.3553	0.3061	0.2842	0.2858	0.2525	0.2713
c_l (deceleration)	0.3306	0.3551	0.3064	0.3032	0.2678	0.2525	0.2712

Table 9. c_l for the optimized Busemann biplane airfoil under lifting conditions at different design points.

4. Conclusions

In this chapter, numerical simulations of the flow past the standard diamond-shaped airfoil and the baseline Busemann-type biplane airfoil have been conducted. An impulsive uniform flow, a flow during acceleration, and a flow during deceleration are simulated. The original Busemann biplane airfoil shows a poor performance under off-design conditions due to the flow-hysteresis phenomenon during acceleration and the choked-flow phenomenon during deceleration. For shape optimization, a single-objective genetic algorithm (SOGA) and a multi-

objective genetic algorithm (MOGA) are employed to optimize the shape of the Busemann-type biplane airfoil under non-lifting and lifting conditions, respectively, to improve its performance under off-design conditions. The commercially available CFD solver FLUENT is employed to calculate the flow field on an unstructured mesh generated using the ICEM grid generation software. A second-order accurate steady-density-based solver in FLUENT is employed to compute the supersonic flow field. The optimization results for the non-lifting case show a significant improvement in reducing the drag coefficient under off-design conditions for the optimized Busemann-type biplane airfoil shape compared to the original shape. The flow-hysteresis phenomenon during acceleration and the choked-flow phenomenon during deceleration are both alleviated significantly for the optimized shape. For the lifting case, the optimized Busemann biplane airfoil is able to significantly reduce the drag coefficient under off-design conditions while generating lift at the same time.

Author details

Yi Tian and Ramesh K. Agarwal*

*Address all correspondence to: rka@wustl.edu

Department of Mechanical Engineering and Materials Science, Washington University in St. Louis, St. Louis, MO, USA

References

[1] Busemann, A., *Aerodynamic Lift at Supersonic Speeds*, 12th ed., No. 6, Luftfahrtforschung, 1935, pp. 210–220.

[2] Moeckel, W. E., *Theoretical Aerodynamic Coefficients of the Two-Dimensional Supersonic Biplane*, NACA Tech. Rept. 1316, 1947.

[3] Licher, R., *Optimum Two-Dimensional Multiplanes in Supersonic Flow*, Douglas Aircraft Co. Tech Dept. SM-18688, 1955.

[4] Tan, H. S., *The Aerodynamics of Supersonic Biplanes of Finite Span*, WADC Tech. Rept. 52-276, 1950. Wright Air Development Center. Dayton, OH.

[5] Ferri, A., *Elements of Aerodynamics of Supersonic Flow*, Macmillan Company, New York, 1949.

[6] Igra, D., and Arad, E., "A Parametric Study of the Busemann Biplane Phenomena," Shock Waves, 16, 3, 2007, 269–273, doi:10.1007/s00193-006-0070-x.

[7] Kusunose, K., Matsushima, K., Goto, Y., Yamashita, H., Yonezawa, M., Maruyama, D., and Nakano, T., "A Fundamental Study for the Development of Boomless Supersonic

http://dx.doi.org/10.5772/62811

Transport Aircraft," AIAA Paper 2006-654, 44rd AIAA Aerospace Sciences Meeting and Exhibit, American Institute of Aeronautics and Astronautics, Reston, VA, 2006.

[8] Maruyama, D., Matsushima, K., Kusunose, K., and Nakahashi, K., "Aerodynamic Design of Biplane Airfoils for Low Wave Drag Supersonic Flight," AIAA Paper 2006-3323, 24th Applied Aerodynamics Conference, 2006; American Institute of Aeronautics and Astronautics, Reston, VA.

[9] Matsushima, K., Maruyama, D., Kusunose, K., and Matsuzawa, T., "Numerical Design and Assessment of a Biplane as Future Supersonic Transport—Revisiting Busemann's Biplane," 25th International Congress of Aeronautical Sciences, ICAS Paper 2006-3.7.1, 2006, pp. 1–10.

[10] Maruyama, D., Matsuzawa, T., Kusunose, K., Matsushima, K., and Nakahashi, K., "Consideration at Off-design Conditions of Supersonic Flows around Biplane Airfoils," AIAA Paper 2007-687, 45th AIAA Aerospace Sciences Meeting and Exhibit, 2007.

[11] Yamashita, H., Yonezawa, M., Obayashi, S., and Kusunose, K., "A Study of Busemann-Type Biplane for Avoiding Choked Flow," AIAA Paper 2007-688, 45th AIAA Aerospace Sciences Meeting and Exhibit, 2007.

[12] Kuratani, N., Ogawa, T., Yamashita, H., Yonezawa, M., and Obayashi, S., "Experimental and Computational Fluid Dynamics around Supersonic Biplane for Sonic-Boom Reduction," AIAA Paper 2007-3674, 13th AIAA/CEAS Aeroacoustics Conference (28th AIAA Aeroacoustics Conference), 2007.

[13] Kashitani, M., Yamaguchi, Y., Kai, Y., and Hirata, K., "Preliminary Study on Lift Coefficient of Biplane Airfoil in Smoke Wind Tunnel," AIAA Paper 2008–349, 46th AIAA Aerospace Sciences Meeting and Exhibit, 2008; American Institute of Aeronautics and Astronautics, Reston, VA.

[14] Maruyama, D., Matsushima, K., Kusunose, K., and Nakahashi, K., "Three-Dimensional Aerodynamic Design of Low-Wave-Drag Supersonic Biplane Using Inverse Problem Method," Journal of Aircraft, 46, 6, 2009, 1906–1918. doi:10.2514/1.40313.

[15] Maruyama, D., Kusunose, K., and Matsushima, K., "Aerodynamic Characteristics of a Two-Dimensional Supersonic Biplane Covering its Take-Off to Cruise Conditions," Shock Waves, 18, 6, 2009, 437–450.

[16] Kusunose, K., Matsushima, K., and Maruyama, D., "Supersonic Biplane," Progress in Aerospace Sciences, 47, 1, 2011, 53–87. doi:10.1016/j.paerosci.2010.09.003.

[17] Hu, R., Jameson, A., and Wang, Q., "Adjoint-Based Aerodynamic Optimization of Supersonic Biplane Airfoils," Journal of Aircraft, 49, 3, 2012, 802–814.

[18] Deb, K., Pratap, A., Agarwal, S., and Meyarivan, T., "A Fast and Elitist Multi-objective Genetic Algorithm: NSGA-II," IEEE Transactions on Evolutionary Computation, 6, 2, 2002, 182–197. doi:10.1109/4235.996017.

[19] He, Y., "Shape Optimization of Airfoils Without and With Ground Effect Using a Multi-Objective Genetic Algorithm," M.S. Thesis, School of Engineering and Applied Science, Washington University in St. Louis, 2014.

[20] "Some Single- and Multiobjective Optimization Techniques," in Unsupervised Classification – Similarity Measures, Classical and Metaheuristic Approaches, and Applications, Chapter 2, 17–21, Springer-Verlag, Berlin, Heidelberg, Bandyopadhyay, S., and Saha, S., 2013. doi: 10.1007/978-3-642-32451-2.

[21] Available from: https://www.math.ubc.ca/~cass/gfx/bezier.html (accessed 9 Dec 2014).

IntechOpen

IntechOpen